ACS APPLIED MATERIALS & INTERFACES

Research Article

Cite This: ACS Appl. Mater. Interfaces 2018, 10, 44011−44017

www.acsami.org

# Toughening Nanoparticle Films via Polymer Infiltration and Confinement

Yijie Jiang,[†,§] Jyo Lyn Hor,[‡,§] Daeyeon Lee,[‡] and Kevin T. Turner*[,†]

[†]Department of Mechanical Engineering and Applied Mechanics and [‡]Department of Chemical and Biomolecular Engineering, University of Pennsylvania, Philadelphia, Pennsylvania 19104, United States

Supporting Information

**ABSTRACT:** Disordered nanoparticle films have significant technological applications as coatings and membranes. Unfortunately, their use to date has been limited by poor mechanical properties, notably low fracture toughness, which often results in brittle failure and cracking. We demonstrate that the fracture toughness of $TiO_2$ nanoparticle films can be increased by nearly an order of magnitude through infiltration of polystyrene into the film. The fracture properties of films with various polymer volume fractions were characterized via nanoindentation pillar-splitting tests. Significant toughening is observed even at low volume fractions of polymer, which allows the nanoparticle packing to be toughened while retaining porosity. Moreover, higher-molecular-weight polymers lead to greater toughening at low polymer volume fractions. The toughness enhancement observed in polymer-infiltrated nanoparticle films may be attributed to multiple factors, including an increase in the area and strength of interparticle contacts, deflection and blunting of cracks during failure, and confinement-induced polymer bridging of nanoparticles. Our findings demonstrate that polymer infiltration is a highly effective route for reinforcing nanoparticle packings while retaining porosity.

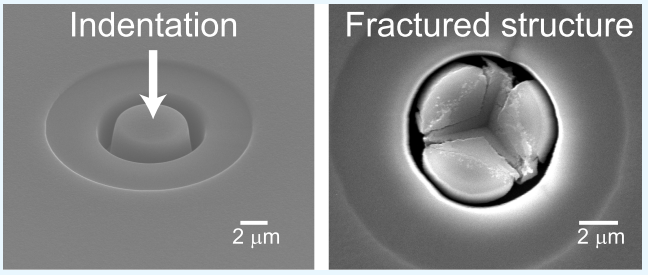


**KEYWORDS:** *polymer-infiltrated nanoparticle film, nanoconfinement, fracture toughness, capillary bridging, micropillar*



## INTRODUCTION

Disordered nanoparticle (NP) films, which have broad applications in energy,[1,2] optics,[3−5] catalysis,[6] sensing,[7,8] and electronics,[9] have low fracture toughness and are thus brittle and highly susceptible to cracking. Due to the weak interparticle bonding in these disordered NP films, mechanical perturbations can easily lead to local particle rearrangements that proliferate quickly and result in the formation of shear bands and cracks.[10] As a consequence of their poor durability and low damage tolerance, NP films have had limited technological impact in many functional systems.[11] Although atomic layer deposition,[12,13] surface functionalization of nanoparticles,[14,15] and incorporation of anisotropic particles[11,16] have been explored as potential routes for improving the mechanical performance of NP packings, none of these techniques have been shown to lead to significant enhancement of fracture toughness.

Natural composite materials, including nacre[17] and tortoise shells,[18] are comprised of a high volume fraction (>60 vol %) of hard and brittle material and a smaller amount of soft polymer. The hierarchical microstructure and composition of these natural composites lead to unique combinations of strength and toughness. Thus, there have been multiple efforts to develop bioinspired materials with enhanced toughness by exploiting combinations of soft and hard materials.[19−22] These prior studies suggest that incorporation of polymers, even in low volume fractions, is a promising route for improving the durability and fracture resistance of assemblies of hard NPs.

Polymer-infiltrated nanoparticle films (PINFs) are NP packings in which the void space is either partially or fully filled by a polymer.[23−28] Several fabrication methods, such as layer-by-layer assembly,[29] spray coating,[30] and polymer solution infiltration,[5] have been used to fabricate PINFs. However, some of these methods, such as layer-by-layer assembly[29] and in situ polymerization,[5,31,32] are time consuming and require complicated process control. Other methods, e.g., spray coating,[30] provide shorter processing times, however, the control of porosity has not been reported in these faster techniques. Undersaturated capillary rise infiltration (UCaRI) is a facile and versatile process to fabricate PINFs.[24] In this technique, thermal annealing is used to infiltrate a nanoparticle packing with a polymer via capillarity and diffusion. The amount of polymer relative to void volume in the NP packing and the duration of thermal annealing can be used to tune the porosity and the compositional gradient of the PINFs, respectively. This allows for control of the morphology, optical, and mechanical properties of the PINFs.[24] Our previous work has demonstrated that by controlling the amount of polymer in the PINF,

Received: September 4, 2018
Accepted: November 21, 2018
Published: December 6, 2018




DOI: 10.1021/acsami.8b15027
ACS Appl. Mater. Interfaces 2018, 10, 44011−44017

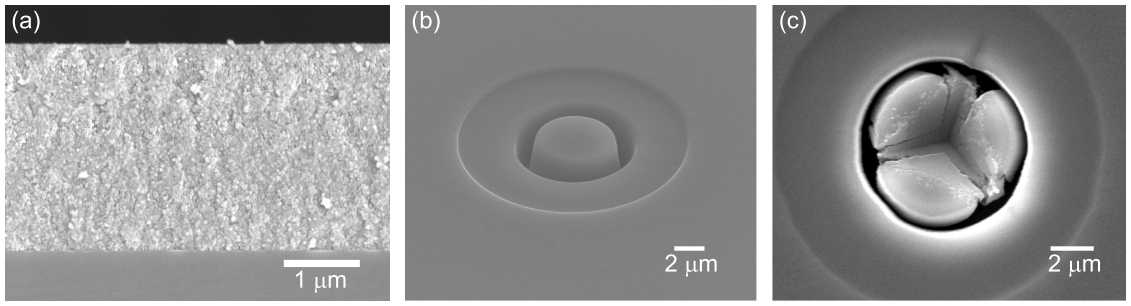


**Figure 1.** SEM images of PINF and micropillars. (a) Cross-sectional SEM image of UCaRI PINF composed of 8k PS and $TiO_2$ nanoparticles ($\phi_{PS}$ = 0.32). (b, c) A FIB-milled micropillar on the same PINF (b) before and (c) after the nanoindentation-based pillar-splitting fracture test.

the elastic modulus can be tuned to be up to ~4.7× and ~2.5× of the pure polymer and neat nanoparticle films, respectively, and the hardness can be tuned up to ~3.5× larger than the constituent materials.[24]

Fracture toughness is a critical material property in any application where a material carries a mechanical load.[33] Yet, it is rarely characterized in studies examining the mechanical properties of NP films. This might be due to challenges in performing fracture toughness measurements on small volume samples, such as in thin films. In particular, conventional fracture toughness measurement techniques for bulk specimens are not readily applied to thin films because the small size makes specimen preparation, crack initiation, and load application challenging.[34] Although nanoindentation-based techniques have been developed for measuring fracture properties of thin films,[35−39] these approaches are mostly applicable only to highly brittle materials. Recently, the micropillar splitting method that allows for toughness characterization on a broader range of materials has been developed.[36] In this technique, the film is first milled into a micropillar using a focused ion beam (FIB), and the critical load for fracture is measured by indenting into the pillar with the sharp Berkovich tip.

In this study, we report the highly nonlinear evolution of the fracture toughness of PINFs generated using UCaRI, composed of ~30 nm titanium dioxide nanoparticles ($TiO_2$ NPs) and polystyrene (PS). We first demonstrate that by varying the volume fraction of PS, the fracture toughness of the UCaRI PINFs can be tuned by up to 9× relative to the neat NP film. Second, we show that increasing the polymer molecular weight generally leads to better enhancement in fracture toughness, especially at low volume fractions of polymer. We also observe large enhancement of fracture toughness in the PINFs, even at low polymer volume fractions (<10 vol %). Thus, UCaRI allows for the fabrication of PINFs with both high porosity and good damage tolerance. We hypothesize that the toughening effect stems from the confinement of polymer upon infiltrating the NP packings, wherein the polymer chains are forced to fit into the narrow pores, thereby bridging multiple NPs to toughen the composite films.

## RESULTS AND DISCUSSION

Nanoporous PINFs composed of ~30 nm $TiO_2$ nanoparticles (NPs) and polystyrene (PS) were fabricated via UCaRI.[24] Specifically, a bilayer structure consisting of a disordered NP layer on top of a PS layer was fabricated via sequential spin-coating, and then the bilayer was thermally annealed above the glass transition temperature of the polymer, resulting in infiltration of the polymer into the voids of the NP packing to form a PINF. The volume fraction of PS, $\phi_{PS}$, in the PINF was kept below the porosity of the NP packing and was controlled by the ratio of the polymer to NP layer thickness, i.e., $\phi_{PS} = h_{PS}/h_{NP}$, where $h_{PS}$ and $h_{NP}$ are the thicknesses of the PS and $TiO_2$ NP layers before annealing.[24]

Nanoporous PINFs films were made with a high volume fraction of nanoparticles ($\phi_{NP} \sim 0.55$) and varying polymer volume fraction ($0.01 \leq \phi_{PS} \leq 0.32$) with corresponding porosity ($p = 1 - \phi_{NP} - \phi_{PS}$) of 0.45−0.13. The molecular weight of the PS in the PINFs was systematically varied, and films with 8k, 173k, and 500k PS were fabricated. Neat PS and neat NP films were also fabricated. The films ranged in thicknesses from 2 to 5 $\mu$m. The uniform distribution of polymer in PINFs made via UCaRI was confirmed using scanning electron microscopy (SEM).

PINF micropillar fracture specimens were fabricated by the FIB milling. Figure 1a,b shows the cross-section of a PINF ($\phi_{PS}$ = 0.32) and a micropillar milled from the PINF, respectively. Pillars with varying radii ($R$ = 1.9−3.6 $\mu$m) were fabricated to ensure that the fracture measurements were insensitive to the pillar radius, while satisfying the geometric constraint that the pillar aspect ratio be sufficiently large, $h/R > 1$,[36] where $h$ is the pillar height. A large shallow circle (Figure 1b) was milled around the pillar to visually facilitate alignment of the indenter to the center of pillars. The pillars were tested in force-controlled nanoindentation experiments with a diamond Berkovich indenter. An SEM image of a fractured pillar is shown in Figure 1c, and typical force−displacement (FD) curves for PINFs with different volume fractions of PS are shown in Figure 2. The jump in displacement in all FD curves indicates unstable crack propagation after a critical load is reached. The critical load, $P_c$, is defined as the load at which this jump in displacement occurs. The pillars split into three parts (Figure 1c), which is due to the geometry of the Berkovich indenter, consistent with prior reports.[36,37,40]

Fracture toughness, $K_{IC}$, is calculated as[36,37]

$$K_{IC} = \gamma \frac{P_c}{R^{3/2}} \quad (1)$$

where $P_c$ is the critical load, $R$ the radius of the micropillar, and $\gamma$ is a dimensionless coefficient related to the elastic modulus and hardness of material, as explained in Materials and Methods. Although the model from which eq 1 is obtained does not account for the influence of residual stress, we show negligible residual stresses in the milled PINF pillars based on a finite element analysis (see Supporting Information) because the free surfaces created during the milling process allow for relaxation of the residual stresses.


DOI: 10.1021/acsami.8b15027
ACS Appl. Mater. Interfaces 2018, 10, 44011−44017

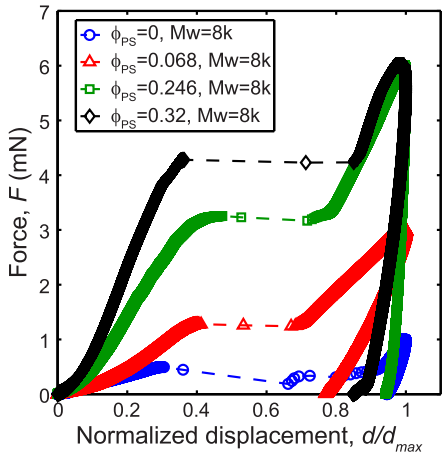


**Figure 2.** Example force−displacement (FD) curves from pillar-splitting tests on PINFs with different volume fractions of 8k PS. The displacement is normalized by the maximum displacement, $d_{max}$, of each indentation test. A jump in displacement indicates fracture of the micropillar at a critical load, $P_c$. The region of FD curve after the jump in displacement is the continued indentation of fractured micropillar and the substrate that completes the preset load function; data from this region of the curve are not used when analyzing the tests.

The fracture toughness of the nanoporous $TiO_2$ NP/PS as a function of $\phi_{PS}$ is shown in Figure 3. By changing $\phi_{PS}$, the PINF fracture toughness can be tuned over nearly an order of magnitude from 0.07 to 0.65 MPa $m^{1/2}$. The fracture toughness of PINFs infiltrated with 8k PS exceeds that of neat PS when $\phi_{PS}$ >0.24. The hardness and modulus of PINFs ($TiO_2$ NP film, infiltrated with 8k PS) increase by a factor of up to 3.5 and 2.5, respectively, relative to the neat NP film, as $\phi_{PS}$ is increased from 0 to 0.35.[24] Thus, by infiltrating NP packings with PS, there are concurrent increases in hardness, stiffness, and most notably fracture toughness. The enhanced fracture toughness of the PINFs relative to the neat PS and neat NP film is attributed to the composition and combination of hard NPs and soft polymer. In PINFs, which are composed predominantly of hard NPs and a soft polymer binder, cracks likely preferentially propagate around the hard nanoparticles

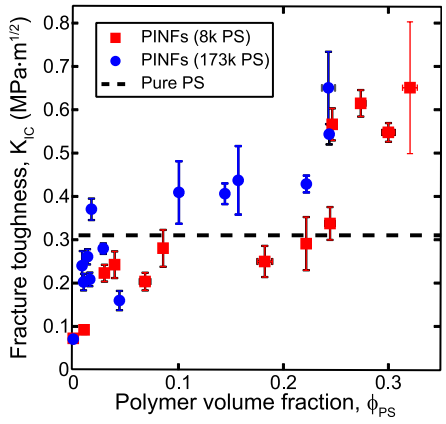


**Figure 3.** Fracture toughness of PINFs filled with 8k PS and 173k PS as a function of polymer volume fraction, $\phi_{PS}$. The dotted line indicates the mean fracture toughness value of the pure 8k and 173k PS films. The error bars represent the standard deviation of uncertainty propagation from experimental measurements (see Supporting Information).

and propagate through the soft PS and/or at the PS−NP interfaces. Deflection of the crack around the hard NPs forces the crack along a tortuous path, resulting in dissipation of additional energy and enhanced toughness.[14,20,41,42]

Importantly, we note a significant increase in the PINF fracture toughness at very low $\phi_{PS}$, when compared with that of the pure NP film. For instance, at $\phi_{PS}$ = 0.03, $K_{IC}$ = 0.25 MPa $m^{1/2}$, which is approximately 3.5 times that of the neat NP film (i.e., $\phi_{PS}$ = 0). This is likely due to formation of polymer capillary bridges at low $\phi_{PS,}$[24,27,43] whereby polymer accumulates preferentially at contact points between NPs, which in turns increases the contact area and strength of the interparticle contacts. Infiltration of nanoparticle packings with polymers was studied previously by molecular dynamic simulations.[24,44] The configuration of the polymer was found to be elongated while infiltrating into narrow pores and to form a bridge between nanoparticles. Experimental observations of such polymer bridging near the contact between nanoparticles were also reported for a similar nanoparticle−polymer composite with larger particles (∼100 nm in diameter).[27] We estimate and compare the contact areas between NPs in a neat NP film and PS−NP contacts in a PINF with $\phi_{PS}$ = 0.03 using analytical models[45] and Surface Evolver (see Supporting Information). We observe up to a ∼146× increase of contact area in the PINF relative to the neat film, which demonstrates why the infiltration of small amount of polymer can significantly enhance fracture toughness of PINFs. This polymer capillary bridge formation is analogous to water in a wet granular material, whereby the capillary condensation of water leads to mechanical reinforcement of granular packings.[46−50] Thus, the PINF toughness can be enhanced significantly via small amount of infiltrated polymer, while still maintaining high porosity.

For $\phi_{PS}$ = 0.03−0.32, the fracture toughness of PINFs (8k PS) increases superlinearly with $\phi_{PS}$, consistent with previous studies on the fracture behavior of porous materials.[52] This may be due to a shift in the dominant toughening mechanism. In particular, the nanoparticles may facilitate crack pinning and deflection[53] leading to an increase in fracture toughness.[54−56] Interestingly, we observe that PINFs generated with higher-molecular-weight polymers show enhanced fracture toughness at lower polymer volume fractions, which we address later in the paper. The fracture toughness of all of the PINFs, regardless of molecular weight, plateau at similar value of $K_{IC}$ ∼ 0.6 MPa $m^{1/2}$ (Figure 3), suggesting that the interfacial bond strength between $TiO_2$ NP and PS is the primary factor that limits the toughness.

SEM images of the indented pillars show that the crack type varies between neat NP films and PINFs, which suggests different underlying mechanisms of deformation. For example, fractured micropillars of neat NP films (Figure 4a) exhibited minimal plastic deformation under the indenter and large through-thickness cracks, similar to radial/median cracks;[55] whereas the $TiO_2$ NP/8k PS PINFs (Figure 4b) had a relatively large plastically deformed area (seen in Figure 4b as a permanent indent that matches the shape of the indenter) and Palmqvist-like cracks. The crack type is known to be directly related to the plasticity[36,57] and fracture toughness.[55] We observe complete fracture of the pure NP pillar (Figure 4a), indicative of a catastrophic, brittle fracture, and low toughness, whereas in the case of the PINF pillar (Figure 4b), the indenter pillar conformed to the indenter tip geometry and appeared to undergo a more homogeneous deformation, a signature of


DOI: 10.1021/acsami.8b15027
ACS Appl. Mater. Interfaces 2018, 10, 44011−44017

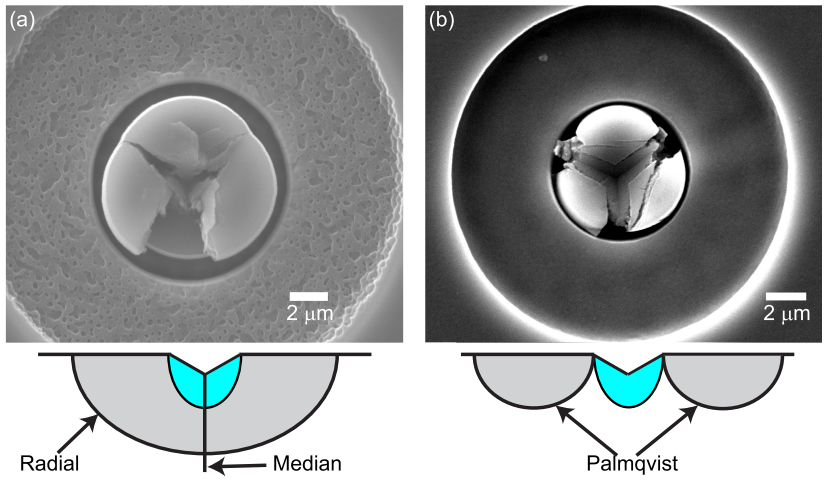


**Figure 4.** SEM images of the fractured micropillars and the schematics of their crack type. (a) Neat nanoparticle film ($\phi_{PS}$ = 0) and (b) a PINF with $\phi_{PS}$ = 0.27. The cracks and plastic zones are represented by gray and blue, respectively.

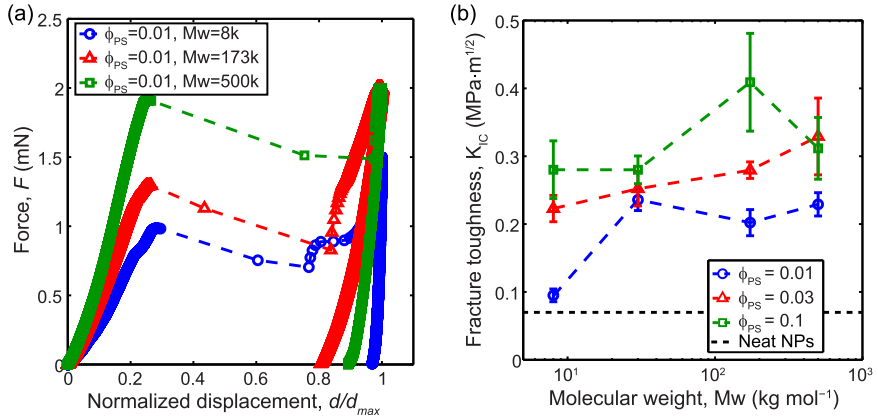


**Figure 5.** Force−displacement curves from pillar-splitting tests on PINFs with (a) different molecular weights of polymer at $\phi_{PS}$ = 0.01. (b) The fracture toughness for PINFs with different polymer volume fractions and molecular weights. The molecular weight varies from 8 to 500 kg/mol and $\phi_{PS}$ = 0.01, 0.03, and 0.1. The error bars represent the standard deviation of uncertainty propagation from experimental measurements (see Supporting Information).

plasticity in the PINF structure.[13,50] The increased plastic deformation (correspondingly, decreased brittle failure) is also observed through lower load drops during unstable crack propagation in micropillars with increasing PS volume fraction in the force−displacement curves (Figure 2).

Another mechanism that may contribute to toughening of NP films via polymer infiltration is nanoconfinement of polymer and bridging of NPs. Recent work found a unique toughening mechanism associated with the physical confinement of polymers.[51] Specifically, polymer chains are forced to stretch to fit into tight pores and as a result cover a larger area of the pore surface. Polymers with higher molecular weight have longer chains, stretch over larger distances, and hence dissipate more energy.[51] One of the advantages of UCaRI is that the method enables the infiltration of polymers that are significantly larger than the characteristic pore size of nanoparticle packings.[58] A high extent of chain confinement (i.e., a high confinement ratio (CR), where CR is defined as the ratio between the radius of gyration of unperturbed polymer chain and average pore radius in nanoparticle packings) requires that the polymer chains stretch and undergo conformational changes to enter the narrow, elongated pores.[27,28] Under such confinement, polymer chains are forced to stretch to fit into tight pores and as a result, will bridge multiple nanoparticles. This NP bridging effect would be increasingly pronounced with increasing CR, which may lead to greater mechanical reinforcement of the PINFs.[59] We tested this hypothesis by varying the molecular weight of the polymer over nearly 2-orders of magnitude (8k−500k), which corresponds to a change in CR from 0.5 to 4. The radius of gyration of polymers, average pore radius in NP and CR of our polymer−nanoparticle system are included in the Supporting Information (see Table S1).

Evidence of confinement-induced toughening is most apparent in PINFs with a low volume fraction ($\phi_{PS}$ = 0.01) of polymers, as seen in Figure 5A. The critical force that induces crack propagation increased by ∼2×, as the molecular weight of PS increased from 8k to 500k. Figure 5B shows the fracture toughness of PINFs as a function of the molecular weight of the infiltrated PS, at various $\phi_{PS}$ of 0.1 and below. All PINFs display enhanced fracture toughness relative to the neat NP film at low $\phi_{PS}$ ($\phi_{PS}$ = 0.01 and 0.03). Consistent with the result at $\phi_{PS}$ = 0.01, enhancement in fracture toughness increases with the infiltrated PS molecular weight, displaying up to 5-fold increase relative to the NP film at these low polymer volume fractions. This is observed even though nanoindentation-based measurements of mechanical properties


DOI: 10.1021/acsami.8b15027
ACS Appl. Mater. Interfaces 2018, 10, 44011−44017

of pure PS thin films are relatively insensitive to the polymer molecular weight[60] (see Figures S3 and S4).

## CONCLUSIONS

In summary, we fabricated and characterized the fracture toughness of nanoporous $TiO_2$ NP/PS PINFs with extremely high NP loading ($\phi_{NP} \approx 0.55$) and varying polymer volume fractions ($0 \leq \phi_{PS} \leq 0.32$). The fracture toughness of the PINFs is significantly higher than that of neat NP film, even at low polymer volume fractions (i.e., $\phi_{PS} < 0.03$). This increase in toughness at low polymer concentrations is attributed to the formation of polymer capillary bridges, which significantly increase the area and strength of the NP contacts. With increasing $\phi_{PS}$, the fracture toughness of the PINFs increases until it plateaus around $K_{IC} \sim 0.6$ MPa $m^{1/2}$. Increasing the molecular weight of the polymer results in a more significant increase in $K_{IC}$ at low $\phi_{PS}$, indicating that PINFs with higher-molecular-weight polymer can tolerate increased deformation with little compromise in its porosity. This study shows that PINFs can be designed, via polymer volume fraction and polymer molecular weight, to achieve desirable fracture properties and porosity for applications such as lightweight composites, separation membranes, and structural coatings.

## MATERIALS AND METHODS

Polystyrene (PS) with four different molecular weights designated 8k ($M_n$ = 8000 $gmol^{-1}$, polydispersity index (PDI) = 1.10), 30k ($M_n$ = 30 000 $gmol^{-1}$, PDI = 1.06), 173k ($M_n$ = 173 000 $gmol^{-1}$, PDI = 1.06), and 500k ($M_n$ = 498 000 $gmol^{-1}$, PDI = 1.08) were purchased from Polymer Source, Inc. $TiO_2$ nanoparticles were synthesized using the hydrothermal method.[61] The major and minor axes of the nanoparticles were 37.4 ± 6.7 and 28.8 ± 4.1 nm, respectively.

**Fabrication of Nanoporous PINFs.** To fabricate the nanoporous PINFs, a recently developed method UCaRI[24] was used. $TiO_2$ NP/PS bilayer films were first prepared, where the PS layer and the $TiO_2$ NP layer were deposited sequentially from their respective solution via spin-coating onto clean 1 × 1 $cm^2$ silicon chips, using a WS-400BZ-6NPP/Lite spin-coater from Laurell Technologies Corporation. The PS solution was prepared by dissolving PS in toluene, whereas $TiO_2$ NPs were dispersed in water. After depositing the PS layer, the PS film was oxygen plasma-treated for ∼2 s to render the film surface hydrophilic, on which the $TiO_2$ NPs layer was spin-coated. The concentration and spin-rate of the solutions depend on the desired film thickness. For PS films in the range of 50−500 nm, 1−11 wt % PS solution was spin-coated at 1000−5000 rpm, whereas PS films 700−900 nm thick, 15 wt % PS solution was spin-coated at 1500−4000 rpm. $TiO_2$ solution (45 wt %) was spin-coated at 1000−1500 rpm to generate $TiO_2$ NP layer. The bilayer films were then annealed above the PS glass transition temperature to infiltrate PS into $TiO_2$ layer and form uniform PINFs.[24] Samples with 8k PS were annealed at 150 °C for 170 h, whereas samples generated with 30k, 173k, and 500k PS were annealed at 170 °C for 340 h. Neat $TiO_2$ NP film and neat PS film were prepared by directly spin-coating 40 wt % $TiO_2$ NP solution at 1000 rpm and 17 wt % PS solution at 1000 rpm, respectively, onto clean silicon wafers.

**Pillar-Splitting Method.** The pillar-splitting method for measuring fracture toughness was first reported by Sebastiani et al.[37] In this method, a micropillar is fabricated, and then a force-controlled indentation test with the Berkovich indenter is performed. The load increases until a critical load, $P_c$, is reached, and an unstable crack propagates causing the pillar to split. The fracture toughness is calculated via eq 1. The coefficient of $\gamma$ can be determined from finite element analysis[36,37] or analytically. Here, we calculate $\gamma$ as

$$\gamma = \frac{\alpha}{0.1859}\sqrt{\frac{E}{H}} \quad (2)$$

where $E$ and $H$ are elastic modulus and hardness measured by nanoindentation on intact PINFs, and $\alpha$ = 0.016 is a geometric parameter for Berkovich indenter.[11,35,62] The derivation to obtain eq 2 is shown in the Supporting Information.

**Fabrication of Micropillars.** The micropillars were fabricated using a FEI Strata DB235 FIB. The micropillars were fabricated by FIB milling with a 30 kV gallium ion beam. All samples were machined first by a 5 nA beam current for rough milling, followed by finer milling steps at lower currents (500 pA to 1 nA). For each PINF, at least five micropillars were milled at randomly selected locations. SEM images were taken after the FIB milling to measure the radii of the micropillars.

**Nanoindentation and Post-Test SEM Observation.** The nanoindentation tests were performed using a Hysitron TI-950 nanoindenter with a diamond Berkovich indenter. The nanoindenter has an optical microscope with magnification of 20−200×. To ensure precision alignment of the indenter with the user identified target, a tip-to-optic calibration was performed before every pillar-splitting indentation test. During the tip-to-optic calibration, a permanent indent on a sample surface (away from micropillars) was made by indenting the Berkovich indenter under 3−5 mN. The optic location was then aligned to the indent position, and the offset between microscope and indenter was therefore calibrated.

Force-controlled nanoindentation tests were performed at a constant loading rate of 200 $\mu$N/s. The force−displacement data were collected at 200 Hz. The critical load for each force−displacement curve was determined as the maximum force before the point where a jump in displacement is observed in the test.

After nanoindentation, SEM images of the pillars were acquired. If the indented location was not aligned near the center of the pillar, or if the nanocomposites delaminated from Si wafer underneath, the data of this pillar were excluded. For each PINF, data were obtained from a minimum of 4, and typically 5, pillars.

## ASSOCIATED CONTENT

### Supporting Information

The Supporting Information is available free of charge on the ACS Publications website at DOI: 10.1021/acsami.8b15027.

Finite element analysis to estimate residual stress in micropillars; derivation of pillar-splitting coefficient $\gamma$; error bar calculations; estimations of interfacial area between two particles after polymer infiltration; confinement ratio of polystyrene within the $TiO_2$ nanoparticle packing; elastic modulus, hardness, and fracture toughness of pure component films.

## AUTHOR INFORMATION


### Corresponding Author

*E-mail: kturner@seas.upenn.edu. Tel: 215-573-7485.

### ORCID

Yijie Jiang: 0000-0002-9347-3290
Jyo Lyn Hor: 0000-0002-0340-8330
Daeyeon Lee: 0000-0001-6679-290X
Kevin T. Turner: 0000-0003-4963-4568

### Author Contributions

§Y.J. and J.L.H. contributed equally.


### Notes

The authors declare no competing financial interest.

## ACKNOWLEDGMENTS

This work was primarily supported by National Science Foundation MRSEC DMR-1720530. Partial support was also provided by the National Science Foundation via CMMI-



DOI: 10.1021/acsami.8b15027
ACS Appl. Mater. Interfaces 2018, 10, 44011−44017

1662695. We also thank Lisa M. Mariani for her assistance with nanoindentation.

## REFERENCES


(1) Pfeiffer, T. V.; Ortiz-Gonzalez, J.; Santbergen, R.; Tan, H.; Schmidt Ott, A.; Zeman, M.; Smets, A. H. M. Plasmonic Nanoparticle Films for Solar Cell Applications Fabricated by Size-Selective Aerosol Deposition. *Energy Procedia* **2014**, *60*, 3−12.

(2) Tricoli, A.; Wallerand, A. S.; Righettoni, M. Highly Porous TiO2 Films for Dye Sensitized Solar Cells. *J. Mater. Chem.* **2012**, *22*, 14254.

(3) Lee, D.; Rubner, M. F.; Cohen, R. E. All-Nanoparticle Thin-Film Coatings. *Nano Lett.* **2006**, *6*, 2305−2312.

(4) Cook, K. T.; Tettey, K. E.; Bunch, R. M.; Lee, D.; Nolte, A. J. One-Step Index-Tunable Antireflection Coatings from Aggregated Silica Nanoparticles. *ACS Appl. Mater. Interfaces* **2012**, *4*, 6426−6431.

(5) Gemici, Z.; Schwachulla, P. I.; Williamson, E. H.; Rubner, M. F.; Cohen, R. E. Targeted Functionalization of Nanoparticle Thin Films via Capillary Condensation. *Nano Lett.* **2009**, *9*, 1064−1070.

(6) Hasan, S. A.; Kavich, D. W.; Dickerson, J. H. Sacrificial Layer Electrophoretic Deposition of Free-Standing Multilayered Nanoparticle Films. *Chem. Commun.* **2009**, 3723.

(7) Soliveri, G.; Ardizzone, S.; Yüksel, S.; Cialla-May, D.; Popp, J.; Schubert, U. S.; Hoeppener, S. Microwave-Assisted Silver Nanoparticle Film Formation for SERS Applications. *J. Phys. Chem. C* **2016**, *120*, 1237−1244.

(8) Choi, J.; Shin, D.; Song, H.; Lee, D.; Kim, K. Current Achievements of Nanoparticle Applications in Developing Optical Sensing and Imaging Techniques. *Nano Convergence* **2016**, *3*, 30.

(9) Millstone, J. E.; Kavulak, D. F. J.; Woo, C. H.; Holcombe, T. W.; Westling, E. J.; Briseno, A. L.; Toney, M. F.; Fréchet, J. M. J. Synthesis, Properties, and Electronic Applications of Size-Controlled Poly(3-Hexylthiophene) Nanoparticles. *Langmuir* **2010**, *26*, 13056−13061.

(10) Cubuk, E. D.; Ivancic, R. J. S.; Schoenholz, S. S.; Strickland, D. J.; Basu, A.; Davidson, Z. S.; Fontaine, J.; Hor, J. L.; Huang, Y.-R.; Jiang, Y.; Keim, N. C.; Koshigan, K. D.; Lefever, J. A.; Liu, T.; Ma, X.-G.; Magagnosc, D. J.; Morrow, E.; Ortiz, C. P.; Rieser, J. M.; Shavit, A.; Still, T.; Xu, Y.; Zhang, Y.; Nordstrom, K. N.; Arratia, P. E.; Carpick, R. W.; Durian, D. J.; Fakhraai, Z.; Jerolmack, D. J.; Lee, D.; Li, J.; Riggleman, R.; Turner, K. T.; Yodh, A. G.; Gianola, D. S.; Liu, A. J. Structure-Property Relationships from Universal Signatures of Plasticity in Disordered Solids. *Science* **2017**, *358*, 1033−1037.

(11) Zhang, L.; Feng, G.; Zeravcic, Z.; Brugarolas, T.; Liu, A. J.; Lee, D. Using Shape Anisotropy to Toughen Disordered Nanoparticle Assemblies. *ACS Nano* **2013**, *7*, 8043−8050.

(12) Dafinone, M. I.; Feng, G.; Brugarolas, T.; Tettey, K. E.; Lee, D. Mechanical Reinforcement of Nanoparticle Thin Films Using Atomic Layer Deposition. *ACS Nano* **2011**, *5*, 5078−5087.

(13) Zhang, D.; Zhang, L.; Lee, D.; Cheng, X.; Feng, G. Reinforcing Nanocolloidal Crystals by Tuning Interparticle Bonding via Atomic Layer Deposition. *Mater. Sci. Eng., A* **2015**, *639*, 514−518.

(14) Chan, K. S.; Lee, Y. D.; Nicolella, D. P.; Furman, B. R.; Wellinghoff, S.; Rawls, R. Improving Fracture Toughness of Dental Nanocomposites by Interface Engineering and Micromechanics. *Eng. Fract. Mech.* **2007**, *74*, 1857−1871.

(15) Lee, D.; Jia, S.; Banerjee, S.; Bevk, J.; Herman, I. P.; Kysar, J. W. Viscoplastic and Granular Behavior in Films of Colloidal Nanocrystals. *Phys. Rev. Lett.* **2007**, *98*, No. 026103.

(16) Rödel, J. Interaction between Crack Deflection and Crack Bridging. *J. Eur. Ceram. Soc.* **1992**, *10*, 143−150.

(17) Katti, K. S.; Katti, D. R.; Pradhan, S. M.; Bhosle, A. Platelet Interlocks Are the Key to Toughness and Strength in Nacre. *J. Mater. Res.* **2005**, *20*, 1097−1100.

(18) Xu, Y.; Zhang, L. Mechanical Properties and Microstructure of Tortoise Shell. *Composites* **1995**, *26*, 315−318.

(19) Munch, E.; Launey, M. E.; Alsem, D. H.; Saiz, E.; Tomsia, A. P.; Ritchie, R. O. Tough, Bio-Inspired Hybrid Materials. *Science* **2008**, *322*, 1516−1520.

(20) Wegst, U. G. K.; Bai, H.; Saiz, E.; Tomsia, A. P.; Ritchie, R. O. Bioinspired Structural Materials. *Nat. Mater.* **2015**, *14*, 23−36.

(21) Das, P.; Malho, J. M.; Rahimi, K.; Schacher, F. H.; Wang, B.; Demco, D. E.; Walther, A. Nacre-Mimetics with Synthetic Nanoclays up to Ultrahigh Aspect Ratios. *Nat. Commun.* **2015**, *6*, No. 5967.

(22) Bouville, F.; Maire, E.; Meille, S.; Van De Moortèle, B.; Stevenson, A. J.; Deville, S. Strong, Tough and Stiff Bioinspired Ceramics from Brittle Constituents. *Nat. Mater.* **2014**, *13*, 508−514.

(23) Huang, Y.-R.; Jiang, Y.; Hor, J. L.; Gupta, R.; Zhang, L.; Stebe, K. J.; Feng, G.; Turner, K. T.; Lee, D. Polymer Nanocomposite Films with Extremely High Nanoparticle Loadings via Capillary Rise Infiltration (CaRI). *Nanoscale* **2015**, *7*, 798−805.

(24) Hor, J. L.; Jiang, Y.; Ring, D. J.; Riggleman, R. A.; Turner, K. T.; Lee, D. Nanoporous Polymer-Infiltrated Nanoparticle Films with Uniform or Graded Porosity via Undersaturated Capillary Rise Infiltration. *ACS Nano* **2017**, *11*, 3229−3236.

(25) Manohar, N.; Stebe, K. J.; Lee, D. Solvent-Driven Infiltration of Polymer (SIP) into Nanoparticle Packings. *ACS Macro Lett.* **2017**, 1104−1108.

(26) Qiang, Y.; Manohar, N.; Stebe, K. J.; Lee, D. Polymer Blend-Filled Nanoparticle Films: Via Monomer-Driven Infiltration of Polymer and Photopolymerization. *Mol. Syst. Des. Eng.* **2018**, *3*, 96−102.

(27) Wang, H.; Hor, J. L.; Zhang, Y.; Liu, T.; Lee, D.; Fakhraai, Z. Dramatic Increase in Polymer Glass Transition Temperature under Extreme Nanoconfinement in Weakly-Interacting Nanoparticle Films. *ACS Nano* **2018**, *12*, 5580−5587.

(28) Hor, J. L.; Wang, H.; Fakhraai, Z.; Lee, D. Effects of Polymer-Nanoparticle Interactions on the Viscosity of Unentangled Polymers under Extreme Nanoconfinement during Capillary Rise Infiltration. *Soft Matter* **2018**, *14*, 2438−2446.

(29) Nolte, A. J.; Rubner, M. F.; Cohen, R. E. Creating Effective Refractive Index Gradients within Polyelectrolyte Multilayer Films: Molecularly Assembled Rugate Filters. *Langmuir* **2004**, *20*, 3304−3310.

(30) Song, L.; Wang, W.; Körstgens, V.; Moseguí González, D.; Löhrer, F. C.; Schaffer, C. J.; Schlipf, J.; Peters, K.; Bein, T.; Fattakhova-Rohlfing, D.; Roth, S. V.; Müller-Buschbaum, P. In Situ Study of Spray Deposited Titania Photoanodes for Scalable Fabrication of Solid-State Dye-Sensitized Solar Cells. *Nano Energy* **2017**, *40*, 317−326.

(31) Flauder, S.; Sajzew, R.; Mu, F. A. Mechanical Properties of Porous $\beta$-Tricalcium Phosphate Composites Prepared by Ice-Templating and Poly($\varepsilon$-Caprolactone) Impregnation. *ACS Appl. Mater. Interfaces* **2015**, *7*, 845−851.

(32) Zhang, H.; Popp, M.; Hartwig, A.; Mädler, L. Synthesis of Polymer/inorganic Nanocomposite Films Using Highly Porous Inorganic Scaffolds. *Nanoscale* **2012**, *4*, 2326−2332.

(33) Launey, M. E.; Ritchie, R. O. On the Fracture Toughness of Advanced Materials. *Adv. Mater.* **2009**, *21*, 2103−2110.

(34) Tsui, T. Y.; Joo, Y.-C. A New Technique to Measure through Film Thickness Fracture Toughness. *Thin Solid Films* **2001**, *401*, 203−210.

(35) Antis, G. R.; Chantikul, P.; Lawn, B. R.; Marshall, D. B. A Critical Evaluation of Indenation Techniques for Measuring Fracture Toughness: I, Direct Crack Measurements. *J. Am. Ceram. Soc.* **1981**, *64*, 533−538.

(36) Sebastiani, M.; Johanns, K. E.; Herbert, E. G.; Pharr, G. M. Measurement of Fracture Toughness by Nanoindentation Methods: Recent Advances and Future Challenges. *Curr. Opin. Solid State Mater. Sci.* **2015**, *19*, 324−333.

(37) Sebastiani, M.; Johanns, K. E.; Herbert, E. G.; Carassiti, F.; Pharr, G. M. A Novel Pillar Indentation Splitting Test for Measuring Fracture Toughness of Thin Ceramic Coatings. *Philos. Mag.* **2015**, *95*, 1928−1944.

(38) Di Maio, D.; Roberts, S. G. Measuring Fracture Toughness of Coatings Using Focused-Ion-Beam-Machined Microbeams. *J. Mater. Res.* **2005**, *20*, 299−302.




DOI: 10.1021/acsami.8b15027
*ACS Appl. Mater. Interfaces* 2018, 10, 44011−44017

(39) Liu, S.; Wheeler, J. M.; Howie, P. R.; Zeng, X. T.; Michler, J.; Clegg, W. J. Measuring the Fracture Resistance of Hard Coatings. *Appl. Phys. Lett.* **2013**, *102*, No. 171907.
(40) Best, J. P.; Zechner, J.; Wheeler, J. M.; Schoeppner, R.; Morstein, M.; Michler, J. Small-Scale Fracture Toughness of Ceramic Thin Films: The Effects of Specimen Geometry, Ion Beam Notching and High Temperature on Chromium Nitride Toughness Evaluation. *Philos. Mag.* **2016**, *96*, 3552−3569.
(41) Ritchie, R. O.; Buehler, M. J.; Hansma, P. Plasticity and Toughness in Bone. *Phys. Today* **2009**, *62*, 41−47.
(42) Meyers, M. A.; McKittrick, J.; Chen, P. Y. Structural Biological Materials: Critical Mechanics-Materials Connections. *Science* **2013**, *339*, 773−779.
(43) Hemmerle, A.; Schröter, M.; Goehring, L. A Cohesive Granular Material with Tunable Elasticity. *Sci. Rep.* **2016**, *6*, No. 35650.
(44) Shavit, A.; Riggleman, R. A. The Dynamics of Unentangled Polymers during Capillary Rise Infiltration into a Nanoparticle Packing. *Soft Matter* **2015**, *11*, 8285−8295.
(45) Derjaguin, B. V.; Muller, V. M.; Toporov, Y. P. Effect of Contact Deformations on the Adhesion of Particles. *J. Colloid Interface Sci.* **1975**, *53*, 314−326.
(46) Leroch, S.; Wendland, M. Influence of Capillary Bridge Formation onto the Silica Nanoparticle Interaction Studied by Grand Canonical Monte Carlo Simulations. *Langmuir* **2013**, *29*, 12410−12420.
(47) Strickland, D. J.; Zhang, L.; Huang, Y.-R.; Magagnosc, D. J.; Lee, D.; Gianola, D. S. Synthesis and Mechanical Response of Disordered Colloidal Micropillars. *Phys. Chem. Chem. Phys.* **2014**, *16*, 10274−10285.
(48) Mitarai, N.; Nori, F. Wet Granular Materials. *Adv. Phys.* **2006**, *55*, 1−45.
(49) Delenne, J. Y.; Richefeu, V.; Radjai, F. Capillary States of Granular Materials in the Funicular State. *AIP Conf. Proc.* **2013**, *1542*, 1023−1026.
(50) Sesso, M. L.; Franks, G. V. Fracture Toughness of Wet and Dry Particulate Materials Comprised of Colloidal Sized Particles: Role of Plastic Deformation. *Soft Matter* **2017**, *13*, 4746−4755.
(51) Isaacson, S. G.; Lionti, K.; Volksen, W.; Magbitang, T. P.; Matsuda, Y.; Dauskardt, R. H.; Dubois, G. Fundamental Limits of Material Toughening in Molecularly Confined Polymers. *Nat. Mater.* **2016**, *15*, 294−298.
(52) Keleş, Ö.; García, R. E.; Bowman, K. J. Deviations from Weibull Statistics in Brittle Porous Materials. *Acta Mater.* **2013**, *61*, 7207−7215.
(53) Faber, K. T.; Evans, A. G. Crack Deflection Processes-I. Theory. *Acta Metall.* **1983**, *31*, 565−576.
(54) Ragosta, G.; Abbate, M.; Musto, P.; Scarinzi, G.; Mascia, L. Epoxy-Silica Particulate Nanocomposites: Chemical Interactions, Reinforcement and Fracture Toughness. *Polymer* **2005**, *46*, 10506−10516.
(55) Chen, J. Indentation-Based Methods to Assess Fracture Toughness for Thin Coatings. *J. Phys. D: Appl. Phys.* **2012**, *45*, No. 203001.
(56) Johnsen, B. B.; Kinloch, A. J.; Mohammed, R. D.; Taylor, A. C.; Sprenger, S. Toughening Mechanisms of Nanoparticle-Modified Epoxy Polymers. *Polymer* **2007**, *48*, 530−541.
(57) Johanns, K. E.; Lee, J. H.; Gao, Y. F.; Pharr, G. M. An Evaluation of the Advantages and Limitations in Simulating Indentation Cracking with Cohesive Zone Finite Elements. *Modell. Simul. Mater. Sci. Eng.* **2014**, *22*, No. 015011.
(58) Hor, J. L.; Wang, H.; Fakhraai, Z.; Lee, D. Effect of Physical Nanoconfinement on the Viscosity of Unentangled Polymers during Capillary Rise Infiltration. *Macromolecules* **2018**, 5069.
(59) Cheng, S.; Bocharova, V.; Belianinov, A.; Xiong, S.; Kisliuk, A.; Somnath, S.; Holt, A. P.; Ovchinnikova, O. S.; Jesse, S.; Martin, H.; Thusitha, E.; Dadmun, M.; Sokolov, A. P. Unraveling the Mechanism of Nanoscale Mechanical Reinforcement in Glassy Polymer Nanocomposites. *Nano Lett.* **2016**, *16*, 3630−3637.
(60) Li, M.; Carter, C. B.; Gerberich, W. W. Nanoindentation Measurements of Mechanical Properties of Polystyrene Thin Films. *MRS Proc.* **2000**, *649*, 1−6.
(61) Sugimoto, T.; Okada, K.; Itoh, H. Synthesis of Uniform Spindle-Type Titania Particles by the Gel-Sol Method. *J. Colloid Interface Sci.* **1997**, *193*, 140−143.
(62) Chen, J.; Bull, S. J. Assessment of the Toughness of Thin Coatings Using Nanoindentation under Displacement Control. *Thin Solid Films* **2006**, *494*, 1−7.


DOI: 10.1021/acsami.8b15027
*ACS Appl. Mater. Interfaces* 2018, 10, 44011−44017